

A photoacoustic patch for three-dimensional imaging of hemoglobin and core temperature

Xiaoxiang Gao

UCSD

Xiangjun Chen

University of Californian San Diego

Hongjie Hu

University of California, San Diego

Xinyu Wang

University of Californian San Diego

Jing Mu

University of Californian San Diego

Zhiyuan Lou

University of Californian San Diego

Ruiqi Zhang

University of Californian San Diego

Keren Shi

University of Californian San Diego

Wentong Yue

University of Californian San Diego

Xue Chen

University of Californian San Diego

Muyang Lin

UCSD <https://orcid.org/0000-0001-6627-6294>

Baiyan Qi

University of Californian San Diego

Sai Zhou

University of Californian San Diego

Chengchangfeng Lu

University of Californian San Diego

Yue Gu

University of Californian San Diego

Hong Ding

University of Californian San Diego

Yangzhi Zhu

University of Californian San Diego

Hao Huang

University of Californian San Diego

Yuxiang Ma

University of Californian San Diego <https://orcid.org/0000-0002-7731-7255>

Mohan Li

University of Californian San Diego

Aditya Mishra

University of Californian San Diego

Sheng Xu (✉ shengxu@ucsd.edu)

University of California San Diego <https://orcid.org/0000-0002-3120-4992>

Article

Keywords: Continuous and Noninvasive Monitoring, Deep Tissues, Ultrasonic Transducers, Vertical-cavity Surface-emitting Laser, Wearable Electronics

Posted Date: July 2nd, 2021

DOI: <https://doi.org/10.21203/rs.3.rs-558432/v1>

License:  This work is licensed under a Creative Commons Attribution 4.0 International License.

[Read Full License](#)

A photoacoustic patch for three-dimensional imaging of hemoglobin and core temperature

Xiaoxiang Gao^{1,*}, Xiangjun Chen^{2,*}, Hongjie Hu^{2,*}, Xinyu Wang¹, Jing Mu², Zhiyuan Lou¹, Ruiqi Zhang¹, Keren Shi², Wentong Yue¹, Xue Chen², Muyang Lin¹, Baiyan Qi², Sai Zhou², Chengchangfeng Lu³, Yue Gu², Hong Ding¹, Yangzhi Zhu¹, Hao Huang¹, Yuxiang Ma¹, Mohan Li¹, Aditya Mishra², Sheng Xu^{1,2,3,4,5,†}

1. Department of Nanoengineering, University of California San Diego, La Jolla, CA 92093, USA

2. Materials Science and Engineering Program, University of California San Diego, La Jolla, CA 92093, USA.

3. Department of Electrical and Computer Engineering, University of California San Diego, La Jolla, CA, USA.

4. Department of Radiology, School of Medicine, University of California San Diego, La Jolla, CA 92093, USA.

5. Department of Bioengineering, University of California San Diego, La Jolla 92093, CA, USA.

*These authors contributed equally to this work.

†Corresponding author. E-mail: shengxu@ucsd.edu

Abstract

Electronic patches, based on various mechanisms, allow continuous and noninvasive monitoring of biomolecules on the skin surface. However, to date, such devices have been unable to sense biomolecules in deep tissues, which have a stronger and faster correlation with the human physiological status. Here, we demonstrate a photoacoustic patch for three-dimensional (3D) mapping of hemoglobin in deep tissues. This photoacoustic patch integrates an array of ultrasonic transducers and vertical-cavity surface-emitting laser (VCSEL) diodes on a common soft substrate. The high-power VCSEL diodes can generate laser pulses that penetrate >2 cm into human tissues and activate hemoglobin molecules to generate acoustic waves, which can be collected by the transducers for 3D imaging of the hemoglobin with a sub-millimeter spatial resolution. Additionally, the photoacoustic signal amplitude and temperature have a linear relationship, which allows 3D mapping of core temperatures with high accuracy and fast response. The results of 3D core temperature mapping and long-term monitoring in ex-vivo and in-vivo studies are validated by commercial devices. With access to biomolecules in deep tissues, this technology adds unprecedented functions to wearable electronics and thus holds significant implications for various applications in both basic research and clinical practice.

Monitoring of biomolecules in the human body can help track wellness levels, diagnose diseases, and evaluate therapeutic outcomes. In particular, the amount and location of hemoglobin in the body provide critical information for perfusion or blood accumulation in that area. Low perfusion in organs or limbs may result in severe shock or amputation¹. On the contrary, accumulation of blood is often a sign of inflammation², trauma³, or cancer⁴. For example, cysts with many possible types of biofluids inside may be found throughout the human body. Bloody cysts are suspicious and should be further examined and closely monitored for the risk of malignant tumors^{5,6}. To enable timely intervention, continuous monitoring of these biomolecules is ideal. However, existing methods are not designed for continuous functioning on individual patients: some necessitate costly equipment, such as magnetic resonance imaging; some rely on radioactive tracers, such as positron emission tomography⁷. Ultrasonography can image internal tissues and blood flow, but requires an operator and a separate lasing system for biomolecule sensing⁸, and is therefore primarily used in a research setting. The recent advances in soft electronics have given rise to soft patches that can adhere to the human skin for continuous health monitoring⁹⁻¹¹. These devices have demonstrated their capability in biomolecule sensing based on electrochemical reactions¹²⁻¹⁹ and optics^{20,21}. However, existing soft patches can only sense biomolecules close to the skin surface. None of them has access to biomolecules in deep tissues, which have a stronger and faster correlation with the physiological and metabolic processes in the human body than those close to the skin surface²² (Supplementary Note 1, Supplementary Table 1).

Here we report a photoacoustic patch for continuous sensing of biomolecules in deep tissues. The device integrates an array of high-power VCSEL diodes and piezoelectric transducers, which are interconnected by serpentine metal electrodes and encapsulated in an elastomeric matrix. Pulsed laser emitted from the VCSEL array excites hemoglobin molecules to radiate acoustic

waves. Those photoacoustic waves will be received by the transducer array and then processed to reconstruct a 3D map of the hemoglobin with a sub-millimeter resolution. Moreover, the photoacoustic signal amplitude has a linear relationship with the media temperature²³. Calibrated photoacoustic signals of hemoglobin enable 3D mapping of core body temperatures with a high spatial resolution. The temperature mapping results generated by the patch show high accuracy and fast response, as validated by commercial core temperature sensors. Finally, we demonstrate the continuous monitoring of the brain temperature under different stimuli to the human body, indicating the potential of this technology for both basic research and clinical practices.

Design, fabrication, and working principle of the soft photoacoustic patch

Figure 1a schematically illustrates the design and working principle of the soft photoacoustic patch. The patch includes a VCSEL array as the light source and a piezoelectric transducer array for photoacoustic wave detection. The laser beams are diffused in deep tissues. Hemoglobin molecules will undergo thermoelastic expansion after absorbing optical energy and collapse when the energy is absent. Therefore, when illuminated by the pulsed laser from the VCSEL array, hemoglobin will vibrate and emit photoacoustic waves. The piezoelectric transducers will receive the photoacoustic waves and generate the spatial distribution of the wave emitters. Therefore, photoacoustic imaging takes advantages of the unique absorption characteristics of biomolecules and highly penetrating acoustic waves to achieve high spatial resolution mapping of biomolecules in deep tissues.

In the patch, 24 VCSELs are evenly distributed in four equally spaced columns (Methods, Figs. S1-S3). The VCSELs in each column are connected in series. The distributed VCSEL layout can help generate uniform illumination in regions below the patch. 240 piezoelectric transducers

are arranged in between the VCSELs, in 15 columns with 16 transducers in each column. To address each transducer independently with a compact device profile, seven layers of serpentine interconnects are designed (Fig. S4). Four adjacent elements in the column are virtually connected in parallel to enhance the signal in the image reconstruction process (Fig. S5), forming 13 linear arrays in the row direction (Fig. S6). The VCSELs, transducers, and interconnects are all encapsulated in an elastomeric polymer, forming an “island-bridge” structure with an overall footprint of $2\text{ cm} \times 1.6\text{ cm}$ and a thickness of 1.2 mm (Methods). In comparison with conventional photoacoustic imaging systems that need complicated components, strict operation environments, and stationary subjects (Supplementary Note 2, Supplementary Table 2), the integrated photoacoustic patch allows convenient imaging on moving subjects.

High power VCSELs, with a peak power of 50 W per diode, are used in this study to achieve a high detection depth and a large signal-to-noise ratio (SNR). A wavelength of 850 nm is used because it has deep tissue penetration and is in the first optical window for probing human tissues^{24,25} (Supplementary Note 3). The receiving transducer element is composed of a piezoelectric layer and a backing layer (Figs. S7-S8). The piezoelectric layer is made of 2 MHz lead zirconate titanate (PZT) micropillars embedded in epoxy. Compared with bulk PZT, the 1-3 composite suppresses the transverse vibration and enhances the axial vibration of the PZT micropillars, thereby increasing the electromechanical coupling coefficient and improving the energy transformation efficiency. The backing layer, made of cured silver epoxy, has a high electric conductivity and a strong attenuation effect on acoustic waves to dampen excessive vibrations and thus improve the signal bandwidth and axial resolution of the transducers.

The as-fabricated soft photoacoustic patch is mechanically and electrically robust. Figure 1b shows the optical photographs of the patch under different modes of deformation, including

bending on a developable surface, wrapping on a nondevelopable surface, and twisting and stretching. Figure 1c presents the infrared camera images of the patch during operation (850 nm laser wavelength). Mechanical deformations do not affect the performance of the VCSELs.

Optical, thermal, and acoustic characterizations of the soft photoacoustic patch

The optical energy distribution in the tissue should be as uniform as possible to minimize systematic artifacts introduced to the photoacoustic images. Optical attenuation needs to be minimal to ensure maximum detection depth. Figure 2a shows the simulated optical intensity in a $2\text{ cm} \times 2\text{ cm} \times 2.5\text{ cm}$ human muscle tissue (Methods). Each VCSEL emits a laser beam perpendicular from the diode surface into the tissue with a divergence angle of 20° . The top surface in Figure 2a corresponds to the interface between the patch and the tissue. The simulated optical intensity distribution in four planes cross-sectioning the illuminated volume is characterized (the bottom panels of Fig. 2a). The optical intensities in the XZ and YZ planes (planes 1 and 2) show uniform distribution in the horizontal direction and small attenuation along the axial direction. In the XY plane, the distributions are highly uniform, with 43% and 10% of the incident intensity at the depths of 1 cm (plane 3) and 2 cm (plane 4), respectively. This indicates the ability of the laser beams to penetrate thick tissue layers.

VCSELs in operation will generate a lot of heat. Excessive heat will not only raise safety concerns, but also degrade the VCSEL performance²⁶. Figure 2b shows the thermal images of the patch on a human arm immediately after turning on the lasers (top panel) and after continuous operation for an hour (bottom panel) at a repetition frequency of 3 kHz and a pulse duration of 200 ns (Figs. S9-S10). After the one-hour operation, the maximum temperature measured was $\sim 36^\circ\text{C}$, slightly higher than the skin surface temperature, but still comfortable for the subject. Figure 2c

presents the changes in incident intensity from the VCSELs during continuous operation. At 3 kHz pulse repetition frequency and 200 ns pulse duration, the intensity decreases by only <4% after one hour, showing the high stability of the VCSELs.

For quantitative photoacoustic studies, it is critical for the transducer array to have a uniform distribution of detection sensitivity to photoacoustic signals in the target region. Figure 2d shows the simulated sensitivity distribution of the transducer array in the $2\text{ cm} \times 2\text{ cm} \times 2.5\text{ cm}$ human muscle tissue, with homogeneously distributed photoacoustic point sources (Methods, Fig. S11). The sensitivity shows high uniformity in the entire 3D space, due to the remarkable penetration of acoustic waves in human tissues. The sensitivity at plane 4 is even slightly higher than plane 3 because the acoustic waves in this study are more focused at this depth. The high detection sensitivity enhances the imaging depth of the photoacoustic patch.

The impulse response is a critical characteristic of a sensing system (Methods, Fig. S12), which is characterized by the time domain photoacoustic signal of a linear source excited by the VCSELs in this study. The working frequency range of the system can be measured by applying the Fourier Transform to the time domain photoacoustic signal (black curve) received by a transducer element generated from a human hair (with a diameter of $\sim 80\text{ }\mu\text{m}$) (Fig. 2e). As the optical intensity of VCSELs is much lower than a conventional bulky laser, photoacoustic signals in the time domain are averaged to increase the SNR. On the other hand, the average times will reduce the frame rate of imaging. To balance the SNR and frame rate in this study, the average times are 3000 (Fig. S13), yielding a frame rate of 1 Hz and an SNR of 19.5 dB (signal of a hair at a depth of 2 cm in a gelatin phantom) at a lasing pulse repetition frequency of 3 kHz. The red curve shows the impulse response in the frequency domain, with a center frequency of 2.40 MHz and a bandwidth of 1.47 MHz (Fig. 2e).

Imaging resolutions are characterized based on a linear source. Photoacoustic images are reconstructed based on signals generated by hairs embedded in gelatin phantoms at different depths. Figure 2f displays a 2D photoacoustic image of a hair at a depth of 2 cm (Methods, Fig. S14). The amplitude profiles of the photoacoustic image in the lateral and axial directions are labeled by the blue and red curves, respectively (the bottom panel). The image resolution is determined by the full width at half maximum (FWHM) of the Gaussian curve fit to the profile. The axial resolution is mainly determined by the signal frequency and remains almost constant at ~ 0.8 mm for different imaging depths (Fig. 2g). The lateral resolution will be reduced from ~ 0.4 mm to ~ 0.7 mm as the imaging depth increases because of the degraded focusing (Fig. 2g).

Ex-vivo 3D hemoglobin mapping

The wavelength of 850 nm is critical for a high penetration depth in human tissues^{24,25} (Supplementary Note 3). Additionally, for photoacoustic mapping of hemoglobin amongst other biomolecules in the tissue, a laser wavelength where hemoglobin absorption is dominant needs to be selected. To characterize the sensing selectivity at this wavelength, we tested cyst phantoms with five different biofluid inclusions, including water, plasma, milk, fat, and bovine whole blood, in transparent colorless silicone tubes embedded underneath a 2 cm thick porcine tissue (Fig. S15). Figure 3a shows the measured optical absorption spectra of all types of biofluids (Methods), which shows that bovine whole blood has the dominant absorption coefficient at 850 nm. To further verify the selectivity, both ultrasound and photoacoustic images of the cyst phantoms are taken (Fig. 3b, Methods). Ultrasound-based B-mode images can only detect the acoustic impedance mismatch between different tissues, which is why the boundaries between the inclusions and matrixes are clear, while the types of biofluids are indistinguishable. The photoacoustic images are based on

the contrast of optical absorptions, which differentiates the blood from other biofluids (Fig. S16).

16 rows of transducers form 13 linear arrays, each of which can produce a 2D photoacoustic image. Combining the 13 images, the patch can generate a 3D map of hemoglobin. The 3D mapping performance is tested on two crossed silicone tubes filled with bovine blood embedded underneath a 2 cm thick porcine tissue. Figure 3c shows a slice of the 3D map where the two silicone tubes overlap (top panel) and the corresponding photoacoustic signal amplitude profile (bottom panel) along the green dashed line in the top panel. The FWHMs of the profiles of these two silicone tubes are computed to be 1.6 and 1.7 mm, respectively, which are close to the inner diameter of the tube (1.2 mm) considering the finite resolution of the photoacoustic system. All 13 slices of the photoacoustic images are displayed in Fig. 3d, where the slice with overlapped tubes in Fig. 3c is highlighted. Figure 3e gives the integrated 3D mapping results of hemoglobin at a depth of 2 cm.

Ex-vivo core temperature mapping and validation

Core temperature is critical for governing the essential functions of the body and should be maintained near 37 °C²⁷. It typically fluctuates within 1 °C according to circadian rhythm²⁸, but can reach ~40 °C amid strenuous workload or ~35.6 °C in extremely cold environments²⁹. A significant deviation of the core temperature indicates failing thermoregulation²⁷ with dire consequences³⁰⁻³³, sometimes life-threatening³⁴. Most of the soft patches can only measure the temperature on the skin surface, which can easily be affected by the external environment and thus has a weak correlation to the core temperature. Noninvasive sensing of core temperature is mainly based on Zero-Heat-Flux^{35,36} or Dual-Heat-Flux^{37,38} thermal models, which have long response times (~3 min)³⁶ and limited detection depths (~1 cm)³⁶ (Supplementary Note 4, Supplementary

Table 3).

Photoacoustic signals are generated when the biomolecules convert the pulsed optical energy to mechanical energy in the form of photoacoustic waves³⁹. In the range of 10 ~ 55 °C, there is a linear relationship between the amplitude of photoacoustic waves and the temperature²³ (Supplementary Note 5), allowing the measurement of temperature by the photoacoustic approach. To test its ability to measure core temperature, we used the soft photoacoustic patch to measure the temperature in a phantom and checked its performance with thermocouples (Fig. 4a). The phantom is composed of warm bovine blood injected in three regions of interest (ROIs) underneath 2 cm thick room-temperature porcine tissues. Thermocouples were placed at the center of each ROI, where the photoacoustic measurements were also taken. Figure 4b shows the relationship between the temperature measured by the thermocouple and the photoacoustic amplitude measured by the patch at ROI 2. The linear fitting of measured data ($R^2 \sim 0.99$) demonstrates the feasibility of core temperature measurements by the patch.

We then studied the patch response to dynamic temperature changes by continuously measuring warm bovine blood as they were injected into the phantom. Upon injection, the temperatures of the three ROIs were close to 32, 36, and 38 °C, which then quickly decreased (Fig. 4c). The measurement results were validated simultaneously by thermocouples (Fig. 4d). Both the photoacoustic patch and the thermocouples have a frame rate of 1 Hz. Bland-Altman analysis of all measurements demonstrates excellent agreement between these two devices (Fig. 4e), indicating the high accuracy and fast response of the photoacoustic patch in measuring core temperatures.

The soft photoacoustic patch can map the temperature distribution with a high spatial resolution. We tested ROI 2, filled with room temperature blood, under a changing thermal gradient

by injecting warm and cold water into ROIs 1 and 3, respectively. The mapping results show that the region close to ROI 1 has a much higher temperature than that near ROI 3 initially (top panel in Fig. 4f); the difference decreases rapidly with time (bottom panel in Fig. 4f). To verify the accuracy of these results, two thermocouples are placed in the ROI 2, labeled as points I and II. The temporal temperature curves measured at these two points show a strong correlation between the thermocouples and the photoacoustic patch (Fig. 4g).

In-vivo continuous monitoring of the brain temperature

The brain temperature depends on a balance of brain metabolism, cerebral blood flow, and external environments⁴⁰. Under the same environmental conditions, fluctuations in the brain temperature can reflect changes in the physiology, function, and even pathology of the brain^{40,41}. Direct measurement of the brain temperature requires the implantation of a temperature probe, which may cause infection and permanent damage to the brain⁴². Many studies have used the temperature of the internal jugular vein (IJV) as an alternative to the brain temperature^{43,44}.

To test the feasibility of in-vivo monitoring, we first used the photoacoustic patch to image a superficial vein on the arm at a depth of ~ 1 mm (Fig. S17). Venous occlusion tests demonstrated the fast response of the photoacoustic patch for in-vivo imaging (Fig. S18). We then applied the photoacoustic patch on the neck to continuously monitor the IJV temperature at a depth of ~ 11 mm (Fig. 5a). The irregular skin curvature has a minimal influence on the imaging resolutions of the photoacoustic patch, due to the relatively low acoustic working frequency (Figs. S19-S20, and Supplementary Note 6). The imaging results are calibrated and validated by a zero-heat-flux model-based commercial core temperature monitoring system. Figure 5b shows 13 slices of photoacoustic images of the IJV superimposed on the corresponding ultrasound B-mode images

(Fig. S21). The carotid artery is invisible in the photoacoustic images because its strong pulsation will induce unstable phases to the photoacoustic signals and therefore skew their coherent averaging^{45,46} (Fig. S22).

We tested the same subject under different stimuli, including ambient temperature rise, sexual arousal, alcohol intake, and physical exercise. Temperatures were simultaneously measured by a photoacoustic patch on the neck, a commercial core temperature sensor on the right side of the forehead, and a skin temperature sensor on the left. The average signal amplitude of the 13 photoacoustic images was used to calibrate against the commercial core temperature sensor. Because the commercial core temperature sensor may have a slower response than the photoacoustic sensor, we only performed the calibration when the physiological status of the subject stabilized (Fig. S23). The photoacoustic measurement data then went through low-pass filtering to remove the high frequency fluctuations.

The brain temperature normally stayed at 37.2 °C without any stimuli (Figs. 5c-5f). When increasing the room temperature from 22.1 to 31.0 °C (Fig. S24), the brain temperature decreased by ~0.5 °C (Fig. 5c), because the elevated ambient temperature causes vasodilation, leading to enhanced cerebral heat dissipation⁴⁷. Meanwhile, the skin temperature increased to a great extent, showing that it is easily affected by the environment and therefore cannot reflect the core temperature accurately. Sexual arousal led to an increase of ~0.6 °C in the brain temperature, and the skin temperature shows the same trend (Fig. 5d). Alcohol intake increases the heat loss through vasodilation⁴⁸ and perspiration⁴⁹, which decreases the core body temperature and the skin temperature, respectively. In this study, the intake of 150 mL 56% liquor decreases the brain temperature by ~0.8 °C at a fast rate of ~0.02 °C/min for the first 30 minutes, then the trend sustained for another 0.2 °C at a slower rate (Fig. 5e). The temperature drop continued for over

100 minutes, which may be due to an overdose of liquor. The intake of a smaller amount (40 mL) showed temperature recovery after 40 minutes (Fig. S25). Figure 5f shows the changes in temperatures during exercise. The subject first kept still to achieve thermostasis. During exercise, the brain temperature quickly rose⁵⁰, at a rate of 0.1 °C/minute, due to the enhanced heat production. When the exercise stopped, the brain temperature quickly decreased at a rate of 0.07 °C/min. In all in-vivo tests, the brain temperatures measured by the commercial device correlate well with the IJV temperatures measured by the photoacoustic patch. The collective results indicate the capability of the soft photoacoustic patch for long-term core body temperature monitoring.

Discussion

The soft photoacoustic patch demonstrated in this study allows for continuous, noninvasive mapping of hemoglobin and core temperature with high spatial resolution in real-time. This is the first report on using soft electronic devices for 3D imaging of biomolecules in deep tissues (>2 cm). The high-resolution imaging of hemoglobin will enable the monitoring of hemodynamics and vascular proliferation in tissues for the management of a variety of conditions and diseases. Quantifying the diameter of blood vessels can be valuable for evaluating vessel functions and diagnosing vascular diseases. For instance, measuring the dynamic change of the vein diameter during an occlusion can help examine venous compliance, which is a strong indicator of cardiac function⁵¹. The photoacoustic effect-based temperature measurements, with advantages of deep penetration, high accuracy, and fast response, introduce a new strategy for monitoring the core temperature, e.g., during exercise, anesthesia, and surgical hypothermia, in fundamental biomedical research and clinical practice^{52,53}.

Although the photoacoustic patch discussed here only detects hemoglobin, this platform technology can potentially be extended to monitor many other endogenous biomolecules, such as melanin^{54,55}, glucose⁵⁶⁻⁵⁸, lipid^{59,60}, cytochrome⁶¹, nucleic acid⁶², and proteins^{63,64}. Furthermore, exogenous contrast agents, like single-walled carbon nanotubes⁶⁵, gold nanoparticles⁶⁶, and methylene blue⁶⁷, can further enhance the signal intensity, increase the detection depth, and improve the detection specificity⁶⁸. The laser wavelength is the key to selectively monitoring various biomolecules. Integrating multiple laser diodes with different wavelengths on the photoacoustic patch can expand the portfolio of detectable biomolecules, with more accurate targeting of biomolecules by detecting a set of absorption characteristics at different wavelengths. The current detection depth is still limited by the optical intensity of the VCSELs. Higher power VCSELs will be needed to further increase the detection depth to the regions of visceral organs. Additionally, higher power VCSELs will be essential for increasing the SNR of photoacoustic signals and thus reduce the average times for imaging dynamic arteries. In the current design, bulky ultrasound probes and sophisticated laser machines are eliminated, which have significantly improved the device portability and ease of use, but a backend system for signal acquisition and processing is still required. Future efforts can focus on minimizing the control electronics to realize a fully integrated wearable system and, therefore, enable measurements on-the-go.

Methods

Fabrication of laser diode chips

The fabrication process of the VCSEL diode chip is schematically illustrated in Figure S2. The anode and cathode of the VCSEL die are on the top and bottom surfaces (Fig. S3), respectively. To facilitate the fabrication of the photoacoustic patch, the anode and cathode are routed to the same surface by creating VIAs and wire bonding. Two vertical openings were created by laser ablation in a 1.7 mm × 2.4 mm × 0.25 aluminum nitride (AlN) substrate and filled with silver epoxy (E-Solder 3022). The silver epoxy VIAs were cured in an oven at 80 °C for 2 hours. The AlN substrate was cleaned with acetone and isopropyl alcohol to remove organic contaminants, followed by rinsing with DI water and drying with nitrogen gas. Moisture induced in the cleaning process was removed by baking the samples in a vacuum oven at 100 °C for 10 min. A lift-off process allowed patterning metal electrodes on AlN. The process involved photolithography (photoresist AZ 1529: spin-casting at 4,000 r.p.m. for 60 s, baking on a hotplate at 95 °C for 120 s, UV irradiance at 350 mJ·cm⁻², and developing for ~40 s with developer AZ 300 MIF) and then sputtering (Ti: 200 W, 3.0 mTorr, 5 sccm Ar, 5 min, ~50 nm; Au: 200 W, 3.0 mTorr, 5 sccm Ar, 15 min, ~400 nm). The sample surface was activated (reactive ion etching: 50 W, 50.0 mTorr, 35–40 °C, 50.0 sccm O₂, 30 s) before sputtering. The samples were soaked in acetone for 30 min to thoroughly remove all photoresists and lift off the metals on the top of the photoresists. Moisture induced in the lift-off process was removed by baking the samples in a vacuum oven at 100 °C for 10 min. The VCSEL die was then pasted on the ground electrode pad on AlN with silver epoxy, which was cured in an oven at 80 °C for 2 hours. The anodes of the VCSEL die and AlN were connected with wire bonding.

Fabrication of the photoacoustic patch

The fabrication process can be generalized into three steps: (1) patterning of the stretchable multilayered electrodes, (2) preparation of the VCSEL diode chips and ultrasonic transducer array, and (3) soft packaging. Cu foils with 20 μm thickness were used as the multilayered conductive interconnects. To adhere the interconnects on the soft elastomeric substrate tightly, a PI thin film [poly(pyromellitic dianhydride-co-4,4'-oxydianiline) amic acid solution, PI2545 precursor, HD Microsystems] was spin-coated on the Cu, at the speed of 4000 r.p.m, with an acceleration of 5000 r.p.m/second, for 60 seconds. The PI was cured by soft baking at 100 °C for 3 minutes and hard baking at 300 °C for 1 hour under a nitrogen atmosphere. The PI-based Cu foil was activated by ultraviolet light (PSD series Digital UV Ozone System, Novascan) for 2 minutes and then laminated on a temporary PDMS substrate (base to hardener ratio is 20:1, Sylgard 184 silicone elastomer). The ultraviolet light activation strengthens the bonding between the PI and the PDMS substrate. A nanosecond laser (Laser Mark's, central wavelength, 1059 to 1065 nm; power, 0.228 mJ; frequency, 35 kHz; speed, 300 mm/s; and pulse width, 500 ns) was used to ablate the Cu/PI into the "island-bridge" serpentine layout. The electrode patterns were designed by AutoCAD (Autodesk, USA). The patterned Cu/PI thin film was transfer-printed to an Ecoflex substrate (15 μm thick; Ecoflex-0030, Smooth-On) on a glass slide using a water-soluble tape (3M) after activation by ultraviolet light for 3 minutes. To tightly stack the second layer of the electrode on top of the first layer, a dielectric layer (15 μm) of Ecoflex was spin-coated on the first layer. Using the same method, six layers of top stimulation electrodes were built up and aligned under the microscope. The VIAs were developed by laser ablation to route all electrodes that were distributed into multiple layers to the same plane. The VCSEL array was bonded with the six-layer electrode using silver-epoxy (Esolder 3022, EIS, USA). Anisotropic conductive films (Elform) were hot

pressed to the front pads of the electrodes to connect the patch to the external power supply and the data acquisition system. The bottom common ground electrode was fabricated in a similar way to the top electrodes.

The structure of the ultrasonic transducer consists of a piezoelectric material and a backing layer. 1-3 PZT-5A composites (Del Piezo, USA) were selected due to their excellent electromechanical coupling coefficients. The condensed backing layer was made of silver-epoxy (Esolder 3022, EIS, USA) for absorbing the extra ultrasonic wave. The silver-epoxy composite was mixed with the hardener in a 12.5:1 ratio over 10 minutes and mounted on a 0.3 mm thick mold, which was then cured at 80 °C for 2 hours. The same silver-epoxy was used to integrate the backing layer with the 1-3 composite material and the entire piece was diced into multiple small elements (0.8 mm length \times 0.6 mm width \times 1 mm thickness).

A scaffold with 240 holes was customized to fix the ultrasonic element arrays. Connections to the top and bottom electrodes were achieved with the conductive adhesive at 80 °C for 2 hours. The device was encapsulated by filling the device with the uncured Ecoflex precursor, followed by curing at 80 °C for 20 minutes. After that, the glass substrates of the top and bottom electrodes were peeled off.

Simulation of optical distribution

The simulation of the optical intensity distribution in a 3D space was performed by the Monte Carlo method using an open-source MATLAB toolbox — MCmatlab⁶⁹. A 4 cm \times 4 cm \times 4 cm homogeneous region was set as the human muscle tissue, with the absorption coefficient μ_a , scattering coefficient μ_s , Henyey – Greenstein scattering anisotropy factor g , and refractive index n set as 0.1 cm⁻¹, 25 cm⁻¹, 0.9, and 1.3, respectively. The region above the top surface was

considered as air, with μ_a , μ_s , g , and n set as $1 \times 10^{-8} \text{ cm}^{-1}$, $1 \times 10^{-8} \text{ cm}^{-1}$, 1, and 1, respectively. The laser diode array was placed at the center of the top surface. The width of each laser source was 1.5 mm. Each laser diode emitted a laser beam into the tissue perpendicular to the surface with a divergence angle of 20° . All the boundaries were set to be cuboid. The wavelength was 850 nm.

Simulation of acoustic detection sensitivity

The simulation of acoustic detection sensitivity was performed in a $4 \text{ cm} \times 4 \text{ cm} \times 4 \text{ cm}$ homogeneous region by a customized MATLAB program. The transducer array was placed at the center of the top surface. The sound speed was set to be 1540 m/s. The simulation region was divided into voxel elements with a pitch of 0.05 mm in each direction. In each voxel, one point source emitted a pulsed photoacoustic signal, expressed as $-2\pi^2 f_0^2 (t - 1/f_0) e^{-\pi^2 f_0^2 (t - 1/f_0)^2}$, where f_0 was 2 MHz. All transducers received the pulse signal, followed by Delay-And-Sum beamforming. The amplitude of the beamformed signal was considered to be the detection sensitivity of this voxel.

System setup and data collection

Verasonics Vantage 256 worked as the host to control the timing sequence of the whole system and signal acquisition. A program was written by MATLAB and run on the Verasonics system, controlling the laser radiation and photoacoustic signal acquisition. To synchronize the laser emission and signal acquisition, Verasonics exported a 3.3 V LVTTTL-compatible trigger signal to the signal generator (Rigol, DG822), which was a 1 μs active low output. The signal generator would be triggered to output a 5 V pulse signal with a duration of 200 ns. The laser driver (PicoLAS) received the output from the signal generator, and immediately provided a 50 A current

to drive the laser diodes with a pulse duration of 200 ns. The peak power of each VCSEL was 50 W driven by a 50 A pulse current. To avoid direct illumination of the thermocouples by the laser beam and getting photoacoustic signals from them, the thermocouples were placed at the peripheral region of the photoacoustic patch. After laser illumination, the Verasonics system started the signal acquisition process. The recorded photoacoustic signal was digitized at a sampling frequency of 62.5 MHz and filtered by a bandpass filter with a center frequency of 2.2 MHz and -6 dB bandwidth of 1.2 MHz. To enhance the SNR, photoacoustic signals were averaged 3000 times to reduce the incoherent noise. Verasonics controlled the VCSELs to emit laser beams and transducers to receive signals at a pulse repetition frequency of 3 kHz, resulting in a detection frame rate of 1 Hz. A C-language program was written and called in MATLAB by the host program to reconstruct the 2D images. The time-domain signals were also saved for offline processing to reconstruct the 3D images.

Image reconstruction algorithms

The Coherence-Factor-weighted-Delay-And-Sum (CFDAS) algorithm was applied to reconstruct photoacoustic images. For the unmodified DAS beamforming algorithm, assuming the photoacoustic signals are measured by a transducer array with M elements, the received signal of each channel is expressed as $p_m(t)$. To reconstruct the image $I(x,z)$ at pixel (x,z) , the wave propagation time from the pixel to the m -th element is calculated as Δt_m . Therefore, the image $I(x,z)$ could be computed through the summation of $\sum_{m=1}^M p_m(\Delta t_m)$. The CFDAS introduces an adaptive coherence factor as an additional weight to $\sum_{m=1}^M p_m(\Delta t_m)$, which is $CF = \frac{|\sum_{m=1}^M p_m(\Delta t_m)|^2}{M \cdot \sum_{m=1}^M |p_m(\Delta t_m)|^2}$.⁷⁰ CFDAS has been demonstrated to improve the image quality⁷¹ (Fig. S14). The reconstructed 2D images were combined in Amira to form 3D images. The gaps between the 2D image slices were

smoothed by Amira automatically.

Test of optical absorption spectra

The NIR-UV-Vis measurements were carried out through a PerkinElmer lambda 1050 UV/Vis/NIR Spectrometer. Water absorbance spectrum was measured under 150 mm InGaAs Int. Sphere Absorbance module and the rest were carried out through 3D WB Det. Absorbance Module. Before each measurement, a 100% transmittance (0 absorbance) baseline was autozeroed. The water spectrum was denoised through white certified reflectance standard from Labsphere Company while the rest background was calibrated with pure water. The detection cuvette had a transmittance length of 5 mm. The injected beam (Slit width of 2.00 nm) was sourced from the combination of D2 Lamp and Tungsten Lamp with a lamp change at 860.8 nm. The spectra were collected in the wavelength range from 1000 nm to 700 nm with a data interval of 1 nm.

Acquisition of ultrasound B-mode images

The ultrasound B-mode images were acquired by the Verasonics Vantage 256 with an L11-5v linear array. The center frequency of the probe was 7.8 MHz. The compounding imaging strategy was applied to reconstruct the images, which transmitted plane waves in 21 directions, received the echoes, and combined them all to form a single image.

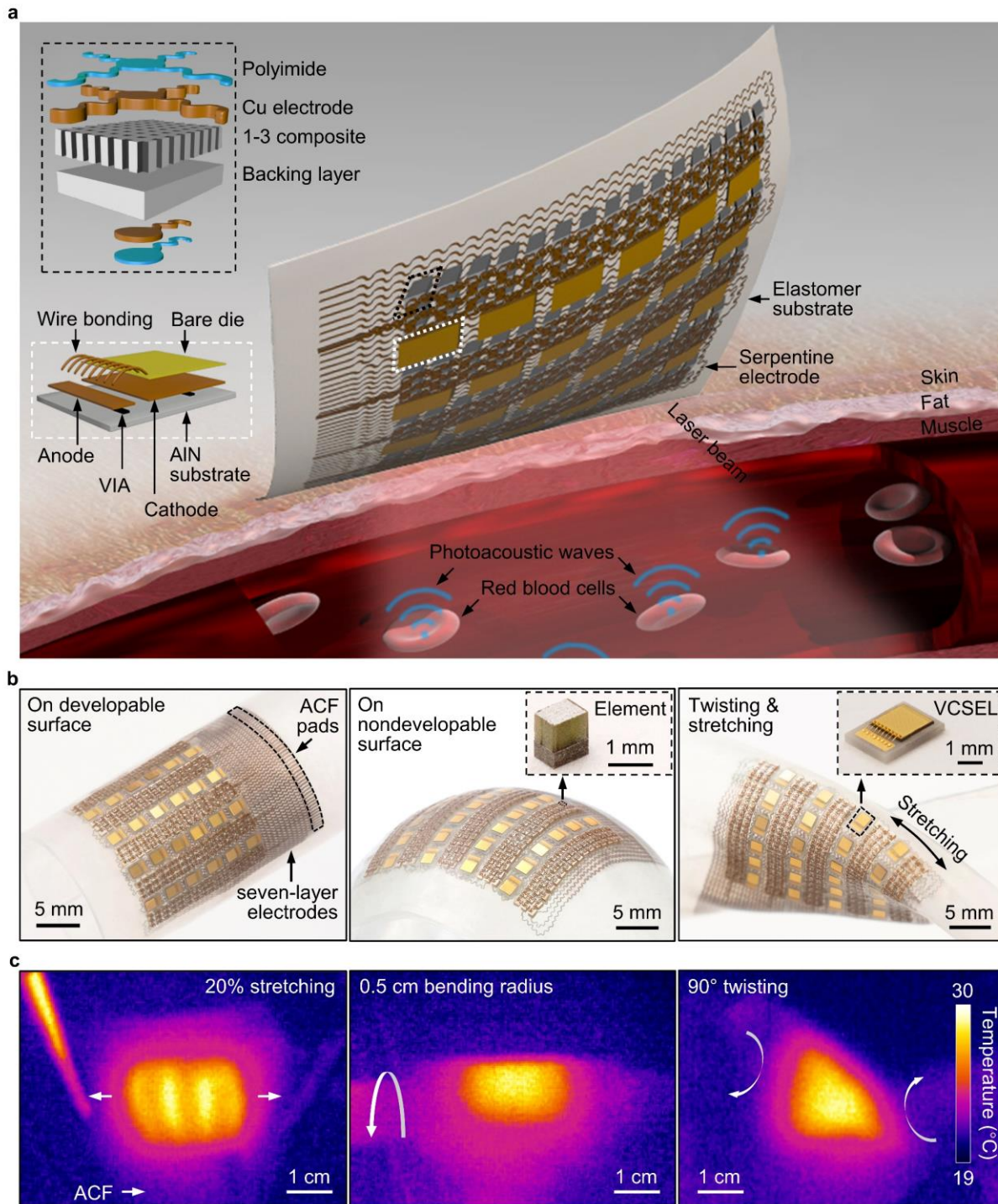


Fig. 1 | Design, fabrication, and working principle of the soft photoacoustic patch. **a**, Schematics of the device structure and the working principle. The patch comprises an array of VCSELs and an array of piezoelectric transducers, interconnected by serpentine Cu electrodes. All components

are encapsulated in Ecoflex. Upon absorption of the optical energy, the hemoglobin molecules in red blood cells undergo thermoelastic expansion and radiate acoustic waves into the surrounding media. The photoacoustic waves will be collected by the transducer array and then relayed to a backend system for data processing. VIA: vertical interconnect access. **b**, Optical photographs of the soft photoacoustic patch under different modes of deformation, including bending on a developable surface, wrapping on a nondevelopable surface, and stretching and twisting. Insets in the middle and right panels are optical micrographs of a single transducer element and a VCSEL diode, respectively. **c**, Infrared camera images of the soft photoacoustic patch when the VCSELs (850 nm laser wavelength) are in operation under different modes of deformation, including stretching, bending, and twisting.

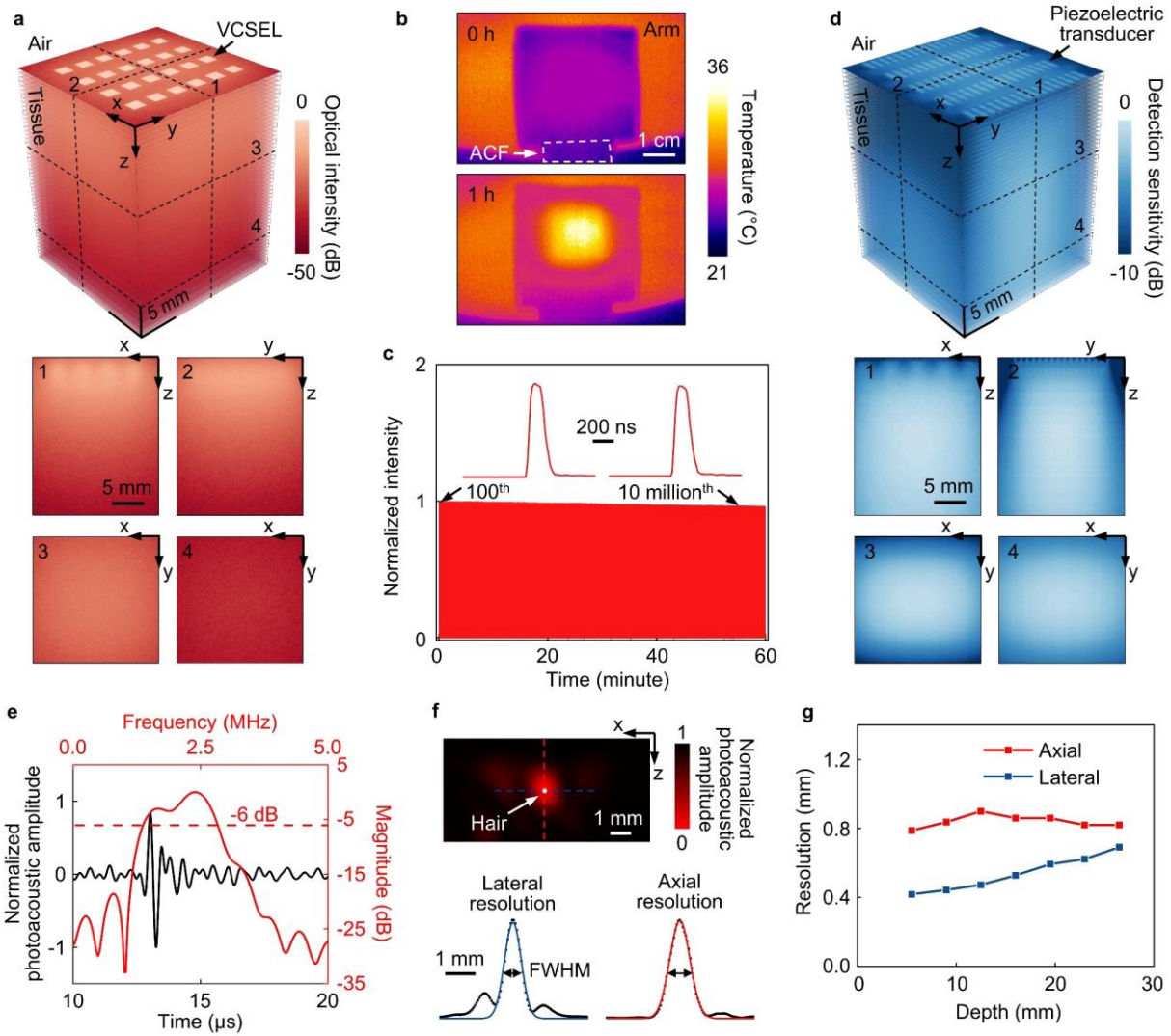


Fig. 2 | Characterizations of the soft photoacoustic patch. **a**, Simulated optical intensity distribution in tissue. The 3D distribution map comprises 51 horizontal planes stacked together with display transparency of 60%. The four slices at the bottom panel highlight the optical intensity distribution at different cross-sections. **b**, Thermal imaging of the photoacoustic patch on the arm immediately after turning on the lasers and after one hour of continuous operation. The maximum temperature is below 36 °C, which is comfortable for long-term wear. **c**, Testing of the VCSELs' output stability as they continuously work for one hour with a pulse duration of 200 ns at a pulse repetition frequency of 3 kHz. The insets correspond to the 100th and the 10 millionth pulses. The

decrease in normalized light intensity after an hour is <4%. **d**, Simulated acoustic detection sensitivity distribution in tissue. The 3D distribution map comprises 51 horizontal planes stacked together with display transparency of 60%. The four slices at the bottom panel highlight the detection sensitivity distribution at different cross-sections. Photoacoustic waves have relatively low attenuation when traveling through tissues and can be detected at large depths. **e**, Photoacoustic impulse response of the patch, in both time and frequency domains, characterized by detecting signal of a hair excited by the VCSELs. **f**, A photoacoustic image of a hair at a depth of 2 cm in a gelatin phantom. The blue and red curves are lateral and axial photoacoustic signal amplitude profiles. The lateral and axial resolutions are determined by the FWHM in different directions. **g**, The lateral and axial resolutions at different depths.

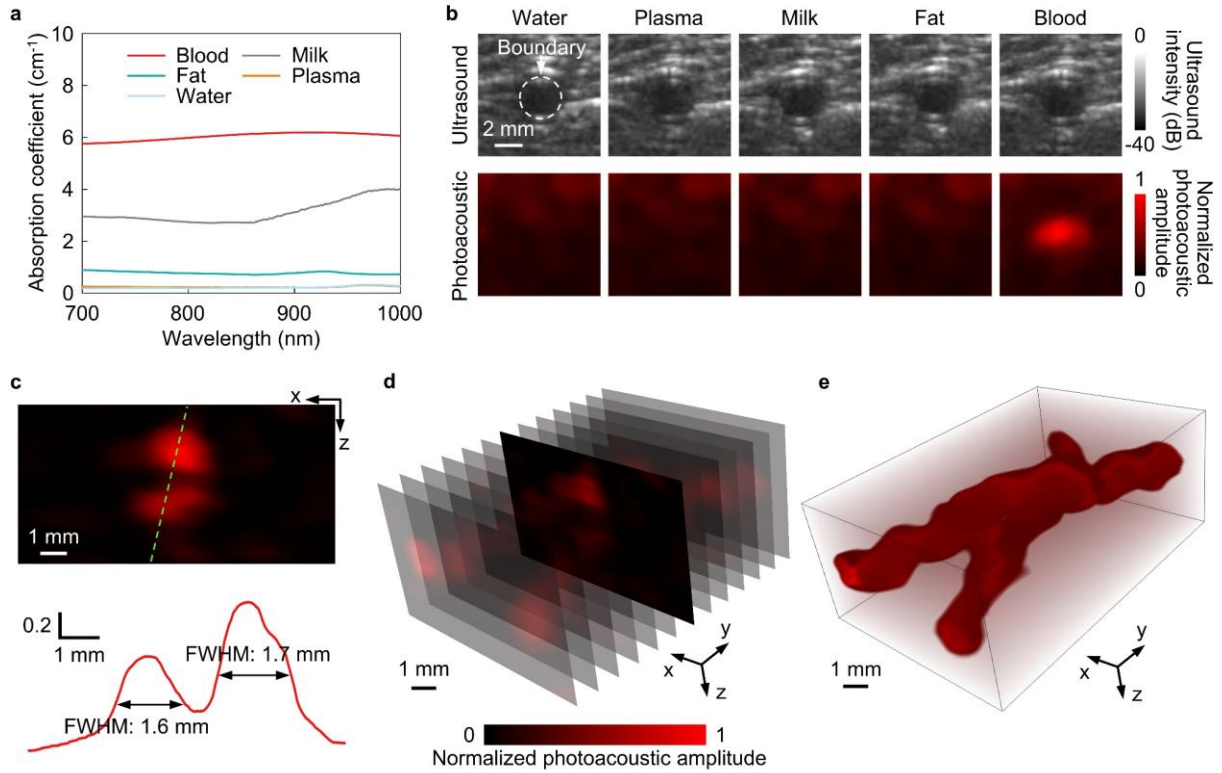


Fig. 3 | Ex-vivo 3D imaging of hemoglobin in deep tissues. **a**, Optical absorption spectra of different body fluids. Absorption coefficients of water, plasma, milk, fat, and bovine whole blood are 0.197, 0.214, 2.716, 0.722, and 6.114 cm^{-1} at the wavelength of 850 nm, respectively. **b**, B-mode and photoacoustic images of different cysts embedded in a porcine tissue at a depth of 2 cm. The B-mode images, acquired by a commercial ultrasound probe, show no differences because of the low acoustic impedance contrast between various fluids. The soft photoacoustic patch differentiates the blood cyst based on the high optical absorption contrast. **c**, A high-resolution photoacoustic image of a blood vessel phantom, which contains two silicone tubes filled with blood embedded underneath a 2 cm thick porcine tissue. The red curve at the bottom panel shows the profile along the green dashed line. The FWHM values are close to the tube's diameter. **d**, 13 slices of photoacoustic images of the blood vessel phantom with display transparency of 80%. **e**, 3D imaging of hemoglobin at a depth of 2 cm.

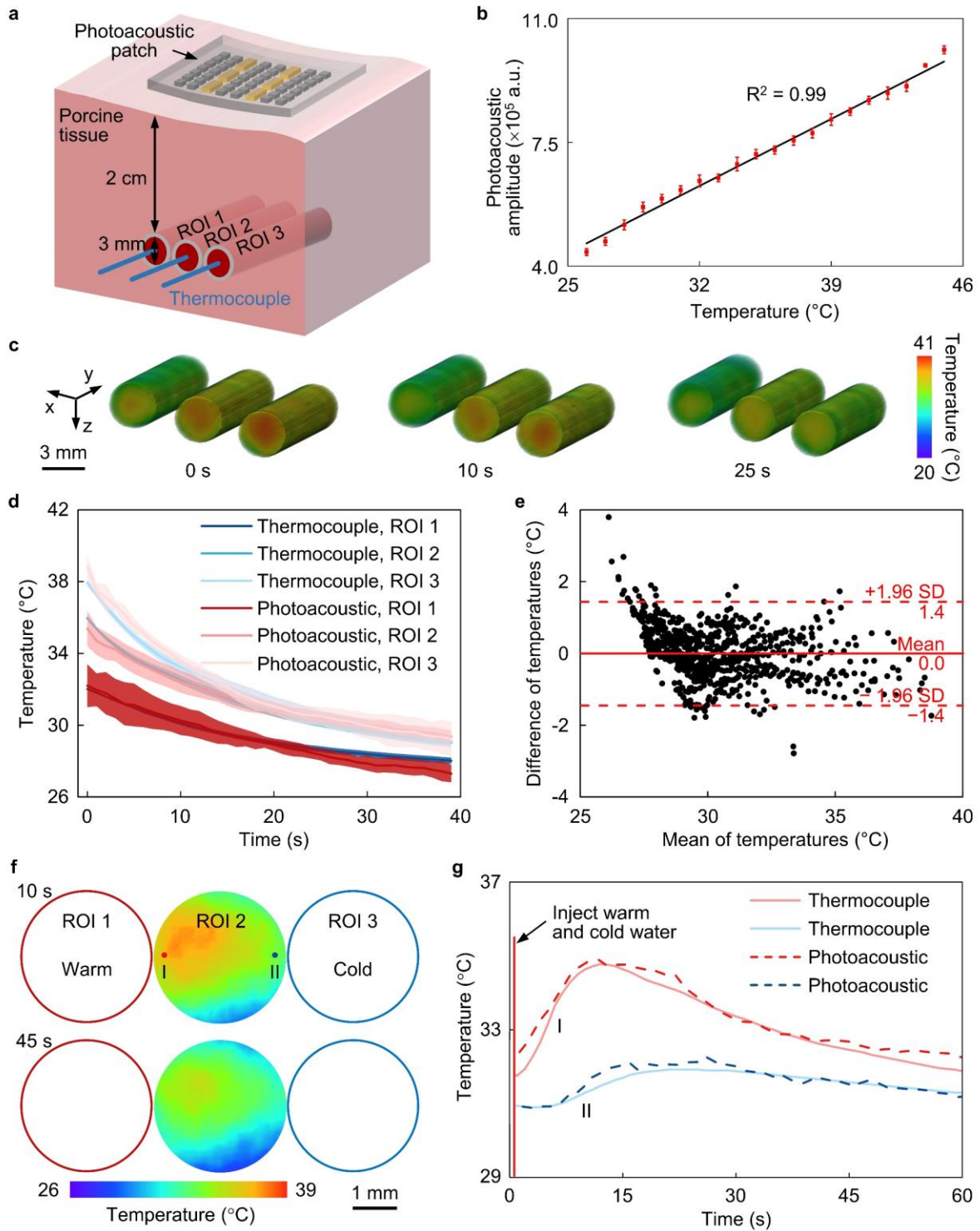


Fig. 4 | Ex-vivo 3D mapping of temperature in deep tissues. a, Schematics showing the corresponding experimental setup. Three silicone tubes, filled with bovine whole blood, are

embedded underneath a 2 cm thick room temperature porcine tissue. Three thermocouples are inserted into each tube to measure the internal temperature simultaneously. **b**, The amplitude of photoacoustic signals at the central point of ROI 2 is extracted to correlate with the temperatures measured by the thermocouple for calibration. **c**, 3D temperature distributions captured by the photoacoustic patch at 0, 10, and 25 s after injecting warm blood into the tubes. **d**, Changes in temperature measured by the photoacoustic patch and the thermocouples. The blue curves are the mean of five thermocouple measurements, and the red curves are the mean of five photoacoustic measurements. The shades of the curves are standard deviations of the measurements. **e**, Bland-Altman plot showing the excellent correlation between the photoacoustic patch and the thermocouple results. The horizontal axis is the mean of the temperatures measured by the two devices, while the vertical axis is the difference between them. **f**, Mapping a changing temperature gradient in real-time using the photoacoustic patch. **g**, Temperature validation curves at points I and II in **f** using thermocouples.

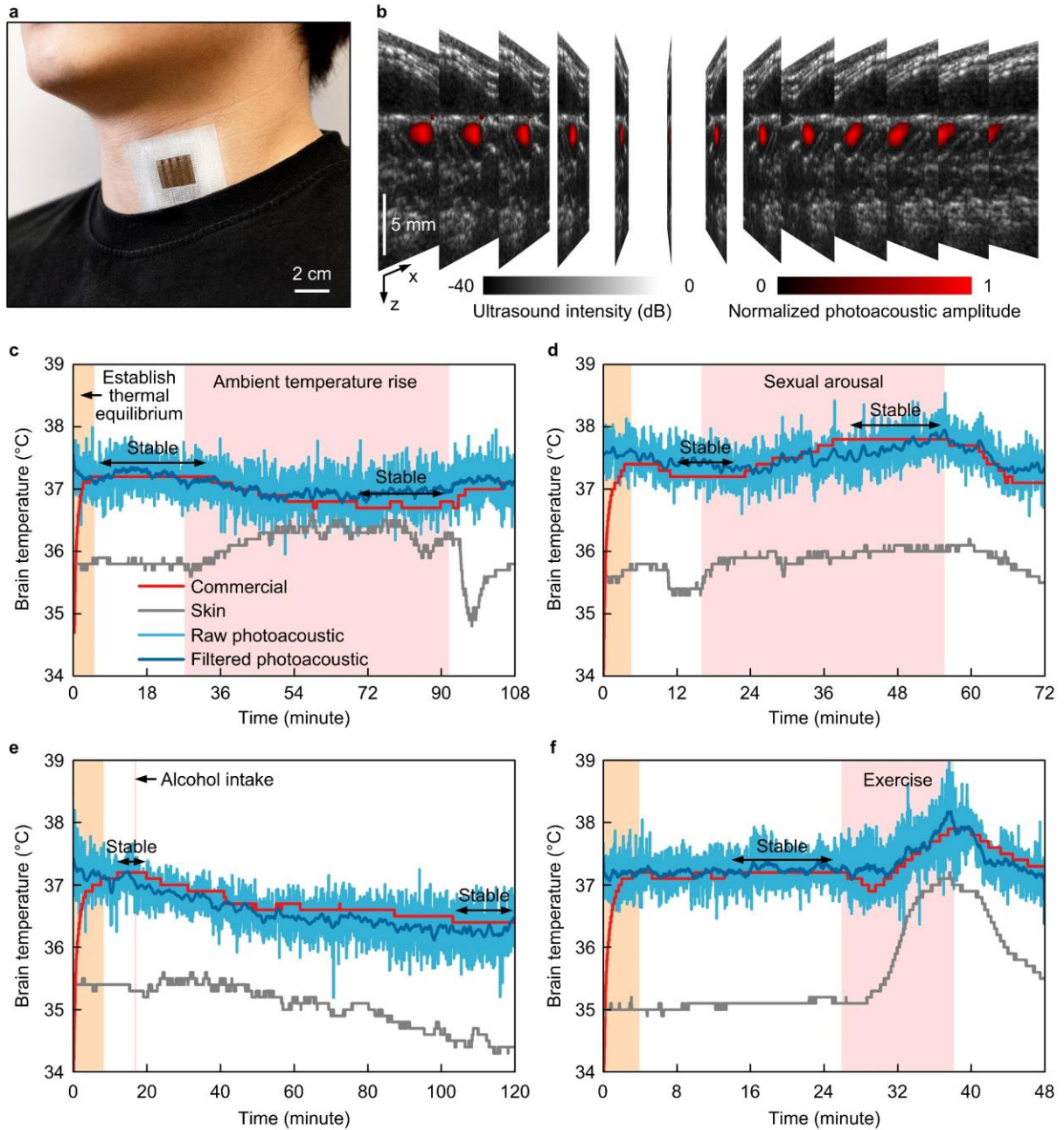


Fig. 5 | In-vivo 3D imaging of IJV and core temperature. **a**, An optical photograph of the patch attached to the human neck at a location above the IJV. **b**, 13 slices of photoacoustic images of IJV superimposed on ultrasound B-mode images. The pixel values of normalized photoacoustic images smaller than 0.5 are not shown. **c-f**, Continuous temperature recording under different stimuli, including **c**, ambient temperature increase, **d**, sexual arousal, **e**, alcohol intake, and **f**, physical

exercise. Curves represent results measured simultaneously by the soft photoacoustic patch (raw data in light blue; data after low pass filtering to remove the high frequency fluctuations in dark blue), commercial core temperature sensor (red), and skin temperature sensor (gray). The orange region represents the time waiting for the commercial core temperature sensor to establish thermal equilibrium. The pink region is when external stimuli are applied. The results of the photoacoustic patch are calibrated by the commercial core temperature sensor during the stable periods.

References

- 1 Bonicolini, E. *et al.* Limb ischemia in peripheral veno-arterial extracorporeal membrane oxygenation: a narrative review of incidence, prevention, monitoring, and treatment. *Crit. Care* **23**, 266 (2019).
- 2 Kriegelstein, C. F. *et al.* Role of blood- and tissue-associated inducible nitric-oxide synthase in colonic inflammation. *Am. J. Pathol.* **170**, 490-496 (2007).
- 3 Rossaint, R. *et al.* Management of bleeding following major trauma: an updated European guideline. *Crit. Care* **14**, R52 (2010).
- 4 Antonescu, C. Malignant vascular tumors--an update. *Mod. Pathol.* **27**, S30-38 (2014).
- 5 Ko, K. H., Kim, E. K. & Park, B. W. Invasive papillary carcinoma of the breast presenting as post-traumatic recurrent hemorrhagic cysts. *Yonsei Med. J.* **47**, 575-577 (2006).
- 6 Kitada, M. *et al.* Surgical treatment of intracystic carcinoma of the breast. *World J. Surg. Oncol.* **9**, 116 (2011).
- 7 Gambhir, S. S. Molecular imaging of cancer with positron emission tomography. *Nat. Rev. Cancer* **2**, 683-693 (2002).
- 8 Wang, L. V. & Yao, J. A practical guide to photoacoustic tomography in the life sciences. *Nat. Methods* **13**, 627-638 (2016).
- 9 Niu, S. M. *et al.* A wireless body area sensor network based on stretchable passive tags. *Nat. Electron.* **2**, 361-368 (2019).
- 10 Bandodkar, A. J. *et al.* Sweat-activated biocompatible batteries for epidermal electronic and microfluidic systems. *Nat. Electron.* **3**, 554-562 (2020).
- 11 Chung, H. U. *et al.* Skin-interfaced biosensors for advanced wireless physiological monitoring in neonatal and pediatric intensive-care units. *Nat. Med.* **26**, 418-429 (2020).
- 12 Kim, J., Campbell, A. S., de Avila, B. E. & Wang, J. Wearable biosensors for healthcare monitoring. *Nat. Biotechnol.* **37**, 389-406 (2019).
- 13 Gao, W. *et al.* Fully integrated wearable sensor arrays for multiplexed in situ perspiration analysis. *Nature* **529**, 509-514 (2016).
- 14 Sempionatto, J. R. *et al.* An epidermal patch for the simultaneous monitoring of haemodynamic and metabolic biomarkers. *Nat. Biomed. Eng.* 1-12 (2021).
- 15 Chen, Y. *et al.* Skin-like biosensor system via electrochemical channels for noninvasive blood glucose monitoring. *Sci. Adv.* **3**, e1701629 (2017).
- 16 Lin, H. *et al.* A programmable epidermal microfluidic valving system for wearable biofluid management and contextual biomarker analysis. *Nat. Commun.* **11**, 4405 (2020).
- 17 Koh, A. *et al.* A soft, wearable microfluidic device for the capture, storage, and colorimetric sensing of sweat. *Sci. Transl. Med.* **8**, 366ra165 (2016).
- 18 Wang, Z. *et al.* Microneedle patch for the ultrasensitive quantification of protein biomarkers in interstitial fluid. *Nat. Biomed. Eng.* **5**, 64-76 (2021).
- 19 Blicharz, T. M. *et al.* Microneedle-based device for the one-step painless collection of capillary blood samples. *Nat. Biomed. Eng.* **2**, 151-157 (2018).
- 20 Yokota, T. *et al.* Ultraflexible organic photonic skin. *Sci. Adv.* **2**, e1501856 (2016).
- 21 Khan, Y. *et al.* A flexible organic reflectance oximeter array. *Proc. Natl. Acad. Sci. U. S. A.* **115**, E11015-E11024 (2018).
- 22 Baca, J. T., Finegold, D. N. & Asher, S. A. Tear glucose analysis for the noninvasive detection and monitoring of diabetes mellitus. *Ocul. Surf.* **5**, 280-293 (2007).
- 23 Shah, J. *et al.* Photoacoustic imaging and temperature measurement for photothermal

- cancer therapy. *J. Biomed. Opt.* **13**, 034024 (2008).
- 24 Shi, L., Sordillo, L. A., Rodriguez-Contreras, A. & Alfano, R. Transmission in near-infrared optical windows for deep brain imaging. *J. Biophotonics* **9**, 38-43 (2016).
- 25 Sordillo, L. A., Pu, Y., Pratavieira, S., Budansky, Y. & Alfano, R. R. Deep optical imaging of tissue using the second and third near-infrared spectral windows. *J. Biomed. Opt.* **19**, 056004 (2014).
- 26 Jasim, F. Z., Omar, K. & Hassan, Z. Temperature effect on VCSEL output performance. *Optoelectron. Adv. Mat.* **3**, 1136-1138 (2009).
- 27 Cheshire Jr, W. P. Thermoregulatory disorders and illness related to heat and cold stress. *Auton. Neurosci.* **196**, 91-104 (2016).
- 28 Coiffard, B., Diallo, A. B., Mezouar, S., Leone, M. & Mege, J. L. A Tangled Threesome: Circadian Rhythm, Body Temperature Variations, and the Immune System. *Biology* **10**, 65 (2021).
- 29 Yousef, H. & Varacallo, M. Physiology, thermal regulation. *StatPearls* (2018).
- 30 Glazer, J. L. Management of heatstroke and heat exhaustion. *Am. Fam. Physician* **71**, 2133-2140 (2005).
- 31 Pozos, R. S. & Danzl, D. Human physiological responses to cold stress and hypothermia. *Medical aspects of harsh environments* **1**, 351-382 (2001).
- 32 Pasquier, M. *et al.* Deep accidental hypothermia with core temperature below 24 degrees c presenting with vital signs. *High. Alt. Med. Biol.* **15**, 58-63 (2014).
- 33 Jardine, D. S. Heat illness and heat stroke. *Pediatr. Rev.* **28**, 249-258 (2007).
- 34 Byard, R. W. & Bright, F. M. Lethal hypothermia – a sometimes elusive diagnosis (Springer, 2018).
- 35 Eshraghi, Y. *et al.* An evaluation of a zero-heat-flux cutaneous thermometer in cardiac surgical patients. *Anesth. Analg.* **119**, 543-549 (2014).
- 36 Pesonen, E. *et al.* The focus of temperature monitoring with zero-heat-flux technology (3M Bair-Hugger): a clinical study with patients undergoing craniotomy. *J. Clin. Monit. Comput.* **33**, 917-923 (2019).
- 37 Huang, M., Tamura, T., Tang, Z., Chen, W. & Kanaya, S. A Wearable Thermometry for Core Body Temperature Measurement and Its Experimental Verification. *IEEE J. Biomed. Health* **21**, 708-714 (2017).
- 38 Kitamura, K. I., Zhu, X., Chen, W. X. & Nemoto, T. Development of a new method for the noninvasive measurement of deep body temperature without a heater. *Med. Eng. Phys.* **32**, 1-6 (2010).
- 39 Wang, L. V. & Hu, S. Photoacoustic tomography: in vivo imaging from organelles to organs. *Science* **335**, 1458-1462 (2012).
- 40 Soukup, J. *et al.* The importance of brain temperature in patients after severe head injury: relationship to intracranial pressure, cerebral perfusion pressure, cerebral blood flow, and outcome. *J. Neurotrauma* **19**, 559-571 (2002).
- 41 Busto, R. *et al.* Small differences in intraischemic brain temperature critically determine the extent of ischemic neuronal injury. *J. Cereb. Blood Flow Metab.* **7**, 729-738 (1987).
- 42 Fountas, K. N. *et al.* Intracranial temperature: is it different throughout the brain? *Neurocrit. Care* **1**, 195-199 (2004).
- 43 Ao, H., Moon, J. K., Tanimoto, H., Sakanashi, Y. & Terasaki, H. Jugular vein temperature reflects brain temperature during hypothermia. *Resuscitation* **45**, 111-118 (2000).
- 44 Kaukuntla, H. *et al.* Temperature monitoring during cardiopulmonary bypass—do we

- undercool or overheat the brain? *Eur. J. Cardiothorac. Surg.* **26**, 580-585 (2004).
- 45 Manwar, R., Zafar, M. & Xu, Q. Signal and Image Processing in Biomedical Photoacoustic
Imaging: A Review. *Optics* **2**, 1-24 (2021).
- 46 Singh, M. K. A., Sato, N., Ichihashi, F. & Sankai, Y. LED-Based Photoacoustic Imaging.
Springer **10**, 978-981 (2020).
- 47 Wang, H. *et al.* Brain temperature and its fundamental properties: a review for clinical
neuroscientists. *Front. Neurosci.* **8**, 307 (2014).
- 48 Johnston, C. E., Bristow, G. K., Elias, D. A. & Giesbrecht, G. G. Alcohol lowers the
vasoconstriction threshold in humans without affecting core cooling rate during mild cold
exposure. *Eur. J. Appl. Physiol. Occup. Physiol.* **74**, 293-295 (1996).
- 49 Desruelle, A. V., Boisvert, P. & Candas, V. Alcohol and its variable effect on human
thermoregulatory response to exercise in a warm environment. *Eur. J. Appl. Physiol. Occup.
Physiol.* **74**, 572-574 (1996).
- 50 Nybo, L. Brain temperature and exercise performance. *Exp. Physiol.* **97**, 333-339 (2012).
- 51 Wilkinson, I. B. & Webb, D. J. Venous occlusion plethysmography in cardiovascular
research: methodology and clinical applications. *Br. J. Clin. Pharmacol.* **52**, 631-646
(2001).
- 52 Kim, J. *et al.* Real-Time Photoacoustic Thermometry Combined With Clinical Ultrasound
Imaging and High-Intensity Focused Ultrasound. *IEEE Trans. Biomed. Eng.* **66**, 3330-3338
(2019).
- 53 Landa, F. J. O., Dean-Ben, X. L., Sroka, R. & Razansky, D. Volumetric Optoacoustic
Temperature Mapping in Photothermal Therapy. *Sci. Rep.* **7**, 9695 (2017).
- 54 Zhang, H. F., Maslov, K., Stoica, G. & Wang, L. V. Functional photoacoustic microscopy
for high-resolution and noninvasive in vivo imaging. *Nat. Biotechnol.* **24**, 848-851 (2006).
- 55 Kim, H. S., Nguyen, V., Bom, H. S. & Min, J. J. In vivo imaging of hemoglobin and
melanin variations using photoacoustic tomography. *J. Nucl. Med.* **56**, 1206-1206 (2015).
- 56 Sim, J. Y., Ahn, C. G., Jeong, E. J. & Kim, B. K. In vivo Microscopic Photoacoustic
Spectroscopy for Non-Invasive Glucose Monitoring Invulnerable to Skin Secretion
Products. *Sci. Rep.* **8**, 1059 (2018).
- 57 Dasa, M. K., Markos, C., Janting, J. & Bang, O. Multispectral photoacoustic sensing for
accurate glucose monitoring using a supercontinuum laser. *J. Opt. Soc. Am. B* **36**, A61-A65
(2019).
- 58 Pleitez, M. A. *et al.* In vivo noninvasive monitoring of glucose concentration in human
epidermis by mid-infrared pulsed photoacoustic spectroscopy. *Anal. Chem.* **85**, 1013-1020
(2013).
- 59 Cao, Y. *et al.* Fast assessment of lipid content in arteries in vivo by intravascular
photoacoustic tomography. *Sci. Rep.* **8**, 2400 (2018).
- 60 Buma, T., Conley, N. C. & Choi, S. W. Multispectral photoacoustic microscopy of lipids
using a pulsed supercontinuum laser. *Biomed. Opt. Express* **9**, 276-288 (2018).
- 61 Zhang, C., Zhang, Y. S., Yao, D. K., Xia, Y. & Wang, L. V. Label-free photoacoustic
microscopy of cytochromes. *J. Biomed. Opt.* **18**, 20504 (2013).
- 62 Shi, J. *et al.* High-resolution, high-contrast mid-infrared imaging of fresh biological
samples with ultraviolet-localized photoacoustic microscopy. *Nat. Photonics.* **13**, 609-615
(2019).
- 63 Li, L. *et al.* Small near-infrared photochromic protein for photoacoustic multi-contrast
imaging and detection of protein interactions in vivo. *Nat. Commun.* **9**, 2734 (2018).

- 64 Mishra, K., Fuenzalida-Werner, J. P., Ntziachristos, V. & Stiel, A. C. Photocontrollable proteins for optoacoustic imaging. *Anal. Chem.* **91**, 5470–5477 (2019)..
- 65 De La Zerda, A. *et al.* Carbon nanotubes as photoacoustic molecular imaging agents in living mice. *Nat. Nanotechnol.* **3**, 557-562 (2008).
- 66 Chen, Y.-S., Zhao, Y., Yoon, S. J., Gambhir, S. S. & Emelianov, S. Miniature gold nanorods for photoacoustic molecular imaging in the second near-infrared optical window. *Nat. Nanotechnol.* **14**, 465-472 (2019).
- 67 Ashkenazi, S. Photoacoustic lifetime imaging of dissolved oxygen using methylene blue. *J. Biomed. Opt.* **15**, 040501 (2010).
- 68 Weber, J., Beard, P. C. & Bohndiek, S. E. Contrast agents for molecular photoacoustic imaging. *Nat. Methods* **13**, 639-650 (2016).
- 69 Marti, D., Aasbjerg, R. N., Andersen, P. E. & Hansen, A. K. MCmatlab: an open-source, user-friendly, MATLAB-integrated three-dimensional Monte Carlo light transport solver with heat diffusion and tissue damage. *J. Biomed. Opt.* **23**, 1-6 (2018).
- 70 Park, S., Karpiouk, A. B., Aglyamov, S. R. & Emelianov, S. Y. Adaptive beamforming for photoacoustic imaging. *Opt. Lett.* **33**, 1291-1293 (2008).
- 71 Liao, C. K., Li, M. L. & Li, P. C. Optoacoustic imaging with synthetic aperture focusing and coherence weighting. *Opt. Lett.* **29**, 2506-2508 (2004).

Acknowledgements

The authors thank Z. Wu for the guidance on the ultrasonic imaging algorithm and data processing, L. Yin for discussions on the laser diode fabrication, D. Yount for discussions on the wire bonding, Y. Chen and Y. Lei for discussions on the ultrasound transducer fabrication, Z. Chen for discussions on data processing, and S. Xiang for the feedback on manuscript preparation. The material is partially based on research sponsored by Air Force Research Laboratory under agreement number FA8650-18-2-5402. The U.S. Government is authorized to reproduce and distribute reprints for Government purposes notwithstanding any copyright notation thereon. The views and conclusions contained herein are those of the authors and should not be interpreted as necessarily representing the official policies or endorsements, either expressed or implied, of Air Force Research Laboratory (AFRL) or the U.S. Government. This work was partially supported by the National Institutes of Health grants 1R21EB025521-01, 1R21EB027303-01A1, and 3R21EB027303-02S1.

Author contributions

X.G., X.J.C., H.J.H., and S.X. designed the research. X.G. and X.J.C. performed the experiments. X.G. performed the data processing. X.G., X.J.C., H.J.H, R.Z., and S.X. wrote the paper. All authors provided constructive and valuable feedback on the manuscript.

Competing interests

The authors declare no competing interests.

Additional information

Supplementary information is available for this paper at

Reprints and permissions information is available at

Correspondence and requests for materials should be addressed to S.X.

Publisher's note: Springer Nature remains neutral with regard to jurisdictional claims in published maps and institutional affiliations.

Supplementary Files

This is a list of supplementary files associated with this preprint. Click to download.

- [GaoSupplementaryinformation.pdf](#)